



Electrochromic graduated filters with symmetric electrode configuration

ALEXANDER HEIN,¹ NIKOLAS LONGEN,¹ FREDERIKE CARL,² JONAS KLEIN,² MARKUS HAASE,² ROMAN STOLL,³ RENATE WARMERS,³ GERALD JENKE,³ CHRISTOPH GIMMLER,⁴ THEO SCHOTTEN,⁴ MICHAEL HAAG-PICHL,⁵ AND EGBERT OESTERSCHULZE^{1,*} 

¹Technische Univ. Kaiserslautern, Erwin-Schrödinger-Str. 46, Kaiserslautern, Germany

²Univ. Osnabrück, Institut für Chemie neuer Materialien, Barbarastr. 7, Osnabrück, Germany

³Matthews International GmbH, Gutenbergstr. 1-3, Vreden, Germany

⁴Fraunhofer-Zentrum für Angewandte Nanotechnologie CAN, Grindelallee 117, Hamburg, Germany

⁵Jos. Schneider Optische Werke GmbH, Ringstr. 132, Bad Kreuznach, Germany

*oester@physik.uni-kl.de

Abstract: Graduated optical filters are commonly used for spatial image control as they are capable of darkening the overexposed parts of the image specifically. However, they lack flexibility because each filter has a fixed transmission distribution. We herein present a fully controllable graduated filter based on the electrochromic device. Its graduated transmission distribution can be spatially controlled by the application of multiple electric potentials. In this way, the control of the gradient's position and its width, transmission and angular orientation is possible. Simulation of both the spatial potential distribution and the resultant optical absorption distribution are conducted to optimize the electrode configuration and furthermore to derive a control dataset that facilitates the adjustment and thus the application of the graduated filter. Based on three objective and quantitative criteria, we identify the electrode configuration with the highest flexibility in all four controls, manufacture the device using a gravure printing process for the nanoparticle electrodes and show its successful application.

© 2020 Optical Society of America under the terms of the [OSA Open Access Publishing Agreement](#)

1. Introduction

In optics, light control is a crucial process to capture images with rich contrast. In quite different applications like laser beam shaping, microscopic imaging or landscape photography, the amount of incident light has to be adapted to the sensor's dynamic range. Since the beginning of the 21st century, the digitalization of imaging along with the introduction of DLSR cameras has led to the development of high dynamic range (HDR) imaging, and increasingly accurate digital postprocessing algorithms [1,2]. However, conventional optical filters remain an important tool for spatial light control as they offer the possibility to influence the light distribution before image capturing with a camera system. Nevertheless, commercially available graduated filters suffer from their prescribed absorption gradient. Thus an adaptation to changing illumination conditions is only possible by mounting a graduated filter with different characteristics.

To overcome this drawback of conventional filter and gain spatial control of the absorption, a group of special materials comes into focus, the so called electrochromic (EC) materials. If they are introduced in an electrochemical cell with a transparent working and counter electrode and an electrolyte in between, they show a potential-dependent transmission, i.e. they can be reversibly colored and bleached by applying an electric voltage [3,4]. This change in transmission relies on the different redox states of the EC materials and a potential-induced redox reaction. Previously, the tunable EC absorption has been used to enhance visibility of an augmented reality display in different lighting conditions [5].

Generally, three different types of EC materials are distinguished: Type I materials are solved in the electrolyte regardless of their redox state. A common example of this group of materials are organic EC molecules such as viologen and phenazine, which have been applied in one of the most popular EC devices; the autodimming rearview mirror by Gentex Corporation [6,7]. Type II materials are in solution when colorless but become solid in their colored state. One example are silver nanoparticles which can be electrodeposited on the electrode by applying a voltage [8,9]. Type III materials are solid both in transparent and colored form and most EC metal oxides like the well-known WO_3 belong to this group [10,11]. Due to their direct contact to the electrode, Type III materials usually show a fast EC response.

We have recently achieved both fast switching and dark coloration with a system of complementary organic molecules which were chemisorbed on transparent nanoporous oxide layers [12]. The chosen molecules were viologen and tetra-*N*-phenylbenzidine (TPB), each equipped with a phosphonate acid anchor group [13–15]. They were immobilized onto TiO_2 and antimony-doped tin oxide (ATO) nanoparticle layers which were chosen to be electrically conductive in the potential range of the redox reaction of the corresponding EC molecule [16,17]. The EC molecules cover the surface of the nanoparticles with a densely packed monolayer [14]. Thus, a nanoparticle layer thickness of a few micrometers enables a suitable absorption to reach a high optical density of up to $\Delta OD = 2$ [12]. The high transmission change could be achieved within only 0.5 s using voltages of ± 1.5 V. This well-balanced system of a cathodically coloring viologen working electrode and an anodically coloring TPB counter electrode provides the basis for our EC filter described hereafter.

Being able to tune the transmission of an optical filter already provides an increased functionality compared to conventional filters. However, in many cases, the illumination of a scene is not homogeneous. The challenge is to darken only the overexposed parts of a scene while keeping the residual image unaffected. We achieved this by introducing an one-dimensional EC graduated filter. Unlike in other EC devices, we did not apply a single potential to the working electrode, but a potential gradient. We demonstrated that the constant current flow along the working electrode between two electrodes created the desired spatial potential distribution $\phi(x)$ [18]. We further showed that the spatially varying transmission T can be analytically derived calculating first the potential dependent concentration of reduced, i.e. colored molecules with Nernst's equation and finally derive the absorption depending on the molecule's individual optical extinction using Lambert Beer's law. We found:

$$T(\phi(x)) = T_0 \cdot \exp\left(\frac{-\epsilon \cdot d}{1 + \exp\left(\frac{zF}{RT_{\text{room}}}(\phi(x) - \phi_{\text{redox}})\right)}\right), \quad (1)$$

which is the basis for the simulation model described below. In Eq. (1), T_0 is the transmission in the transparent state, ϵ and d are the extinction coefficient and the layer thickness, R is the universal gas constant, T_{room} is the room temperature, z the number of electrons transferred in the redox process, F the Faraday constant and ϕ_{redox} is the reaction's redox potential. In this paper, we will show that by creating a two-dimensional potential distribution $\phi(x, y)$ across a homogeneous and transparent working electrode, we can spatially control the transmission and thus create the desired two dimensional gradient. We characterize several electrode configurations to find a setup which can create all four desired functions: translation, stretching, absorption change and rotation of the gradient.

2. Results and discussion

Figure 1 shows the detailed set-up of our device: Instead of structuring the underlying conductive ITO layer of the round working electrode or even its optical active layer to create individually controllable patches or pixels like in a LCD display, we keep the optical area completely

unstructured. Thus, any continuous potential distribution $\phi(x, y)$ defined on this electrode renders a continuous graduated transmission distribution by means of Eq. (1) possible. We use eight individually controllable contact pads for the definition of $\phi(x, y)$. They are equally spaced on the circumference of the round working electrode and lead to ohmic currents in the working electrode. This electrode geometry ensures rotational symmetry. The width of the contact pads, expressed as the angle α in Fig. 2(a), needs to be adapted to obtain the most promising absorption distribution as will be explained below.

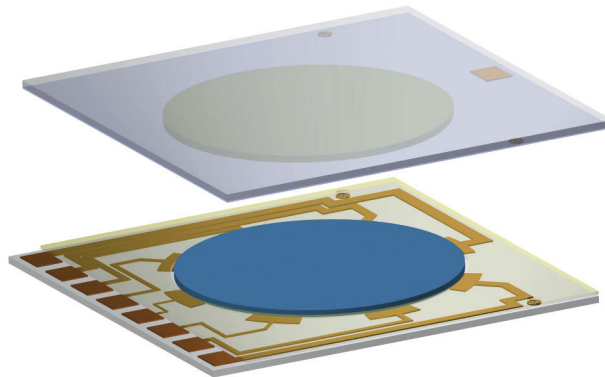


Fig. 1. Cross-section of the graduated filter device consisting of the working electrode with phosphonated viologen on TiO_2 nanoparticles (bottom, shown as blue colored disc) and the counter electrode with TPB on ATO nanoparticles (top, shown as green colored disc). Both EC electrodes use type III materials which are solid in both their transparent and opaque form to avoid migration of the EC species. On the working electrode, eight individually controllable Au contact pads are established on the circumference of the round optical area ($\varnothing = 40$ mm). Owing to the ohmic resistance of the ITO layer on the glass substrate, the lateral current flow allows to create the two-dimensional potential distribution on the working electrode with respect to the counter electrode. This results in a local coloration of the EC materials and the desired continuous graduated transmission distribution.

By controlling the eight potentials, a wide variety of two-dimensional transmission distributions can be generated. However, only the distributions with an one-directional gradient are in the focus of this paper. The g -axis defines the gradient's direction as shown in the simulation model in Fig. 2(a)). With just four parameters all possible one-directional transmission gradients can be described explicitly: The angle θ gives the angle between the g and the y -axis. Along this g -axis we create a gradient keeping the maximum transmission T_{\max} fixed while varying the minimum transmission T_{\min} . The translation of a given gradient is defined by the radial shift g_0 of the point of medium transmission $(T_{\max} - T_{\min})/2$ with respect to the center of the filter. Finally, the width of the gradient's transition zone is given by the parameter Δg .

Combining finite element simulations (Comsol Multiphysics Version 5.4) with the transmission-potential distribution given in Eq. (1), we are able to calculate the transmission distribution T_{sim} for a given set of potentials at the eight contacts. We improved these simulations using an optimization algorithm (bound optimization by quadratic approximation) to find the potential combination and thus the T_{sim} which fits best to the specified transmission distribution T_{spec} described by g_0 , Δg , T_{\min} and θ . By simulating a vast set of parameter combinations, we obtain four-dimensional look-up tables for each of the eight contacts and a resultant T_{sim} for each combination. However, these T_{sim} differ from their corresponding T_{spec} . A reduction of their deviation is feasible by optimizing the opening angle α of the chosen electrode pads. Therefore,

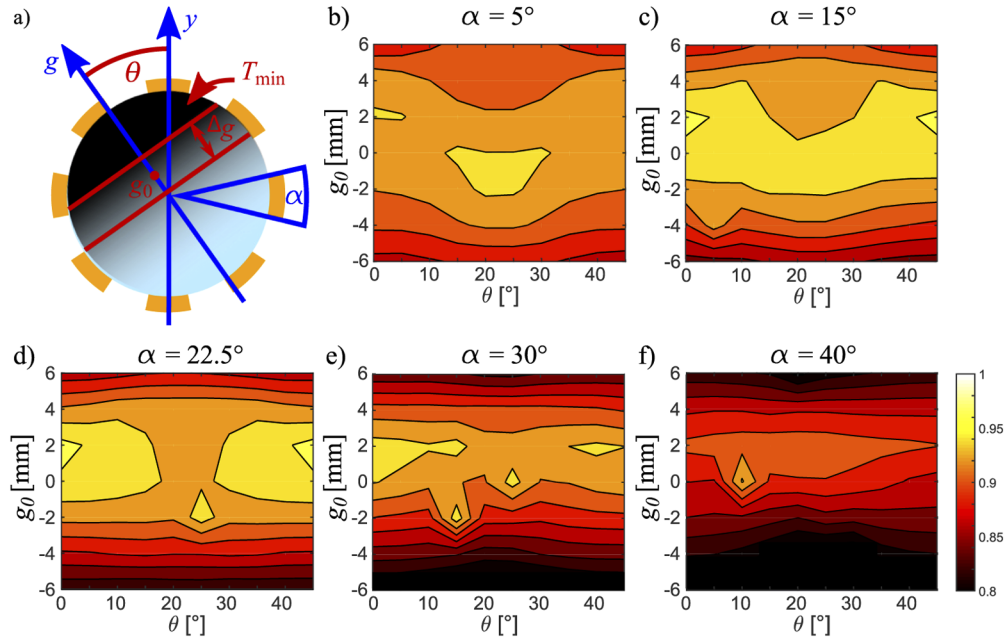


Fig. 2. Definition of the gradient's parameters and the electrode contact angle α (a) and correlation maps for the five different values of α indicated at the top of each image ((b)-(f)). We varied g_0 and θ while keeping $\Delta g = 10$ mm and $T_{\min} = 10\%$ fixed.

we calculated the coefficient of determination

$$R^2 = 1 - \frac{\sum_{x,y} (T_{\text{sim}} - T_{\text{spec}})^2}{\sum_{x,y} (T_{\text{spec}} - \overline{T_{\text{spec}}})^2} \quad (2)$$

for five different values of α as a first criterion for the quality of the simulations. By varying the parameters g_0 and θ , we obtain five arrays with 7×10 entries. Each of the entries correspond to one simulation of the transmission distribution.

When analyzing the results of Fig. 2, we first consider the mean correlation for the five values of α . While the three smallest α reach $\overline{R^2} \geq 0.91$, the coefficient of determination drops to $\overline{R^2} = 0.88$ and even $\overline{R^2} = 0.84$ for $\alpha = 30^\circ$ and $\alpha = 40^\circ$, respectively. Broad contact pads therefore deteriorate the overall quality of the transmission distribution.

When comparing the spatial correlation maps of the remaining three electrode configurations, we find that high correlation values are not evenly distributed: A broad band of high correlation can be found for g_0 in the range of $[-1 \text{ mm}, +3 \text{ mm}]$, while θ has rather low influence on the correlation. If g_0 is close to the edges, the correlation drops. For $\alpha = 5^\circ$, this decrease is less than for $\alpha = 15^\circ$ and $\alpha = 22.5^\circ$. However, the highest values of R^2 are reached for medium g_0 at $\alpha = 15^\circ$ or $\alpha = 22.5^\circ$.

To explain this phenomenon, we take a closer look at the computed spatial transmission distribution. In Fig. 3 the values $g_0 = +2$ mm and $\theta = 0^\circ$ were chosen, which refer to the point of highest correlation in Fig. 2(d). The specification is defined as two flat levels of high and low transmission and a linear transition zone in between. The simulated profiles (b) - (f) show continuous slopes owing to Eq. (1). When comparing the results of the five different electrode configurations, we see that for $\alpha = 5^\circ$ the transition is very broad, i.e. the value of $\Delta g = 10$ mm is exceeded. This is the main reason why the high correlation values can not be reached with

$\alpha = 5^\circ$. As all contact pads are very small, the pads located at the bisectors do not have a sufficient impact on the potential distribution to keep the transmission at its low or high level. Therefore, these levels are smaller than in the specification leading to a lower value of R^2 .

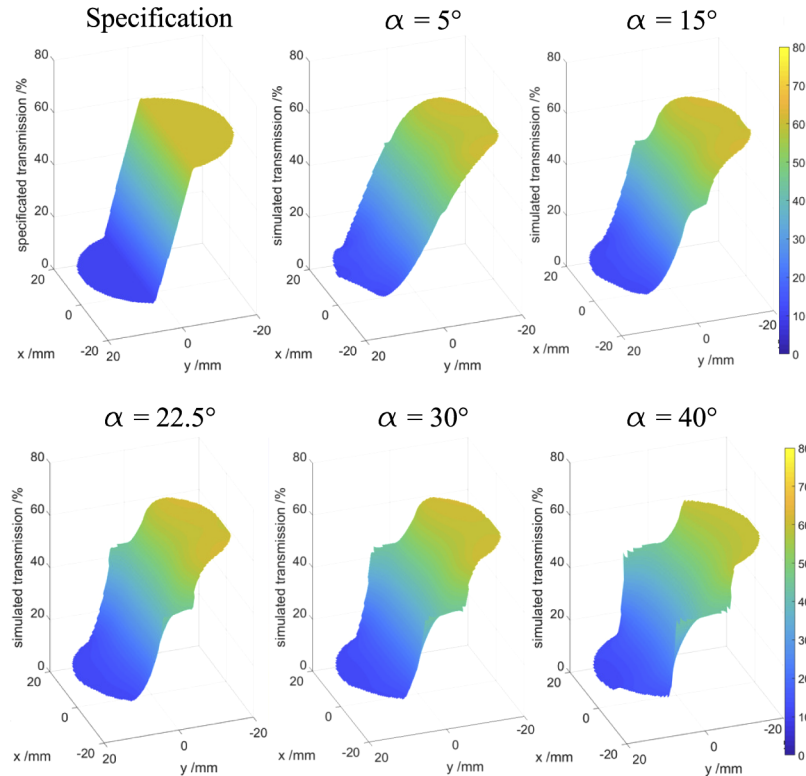


Fig. 3. Spatial transmission distribution across the round active optical area displayed as color coded surface. The upper left diagram shows the specification for $g_0 = +2$ mm, $\Delta g = 10$ mm, $T_{\min} = 10\%$ and $\theta = 0^\circ$.

When α is increased, the influence of each contact pad on the potential distribution and thus on the transmission distribution increases. This becomes evident when observing the edges of the diagrams: Close to the contact pads, an area of homogeneous transmission is created which appears as unwanted steps in the continuous gradient. For $\alpha = 40^\circ$ these steps become so broad that the simulated transmission at the edges significantly differs from the specification, which is the reason for the low average R^2 in Fig. 2(f)). However, medium values for α such as $\alpha = 22.5^\circ$ appear as a good compromise between these two extremes which is confirmed by the steep and simultaneously steady gradient in the diagram.

Another method for quantification of the different electrode designs' quality is matching the position of each gradient in simulation and specification. The accordance of $g_{0\text{sim}}$ and θ_{sim} to the specified values g_0 and θ gives us two additional objective criteria for the quality of the simulations. To find $g_{0\text{sim}}$ and θ_{sim} , we first determined the transmission value at the point of medium transmission $T(g_{0\text{sim}})$. We then identified all points with $|T(x, y) - T(g_{0\text{sim}})| < 1\%$ and projected them into the x - y plane. Finally, these points were fitted to obtain a straight line. This way, we could calculate θ_{sim} as the inclination of this straight line with respect to the x -axis and $g_{0\text{sim}}$ as the minimum distance of this line to the center.

Figures 4 and 5 show the difference of $g_{0\text{sim}}$ and θ_{sim} to the specified values, respectively. Each point in Fig. 4 can be understood as the deviation of $g_{0\text{sim}}$ for the given α at the specified

parameters g_0 and θ . For example, in the diagram for $\alpha = 40^\circ$, a dark blue coloration in Fig. 4 is found at $g_0 = -6$ mm and $\theta = 25^\circ$. This means that $g_{0\text{sim}}$ is significantly lower than the specified -6 mm, i.e. the point of medium transmission is shifted too far to the bottom with a value of $g_{0\text{sim}} = -10.1$ mm. Additionally, we can find the deviation of θ_{sim} in Fig. 5 at the same point in the diagram for $\alpha = 40^\circ$. The light blue color indicates a value of $\theta_{\text{sim}} = 22.8^\circ$ that is lower than the expected 25° .

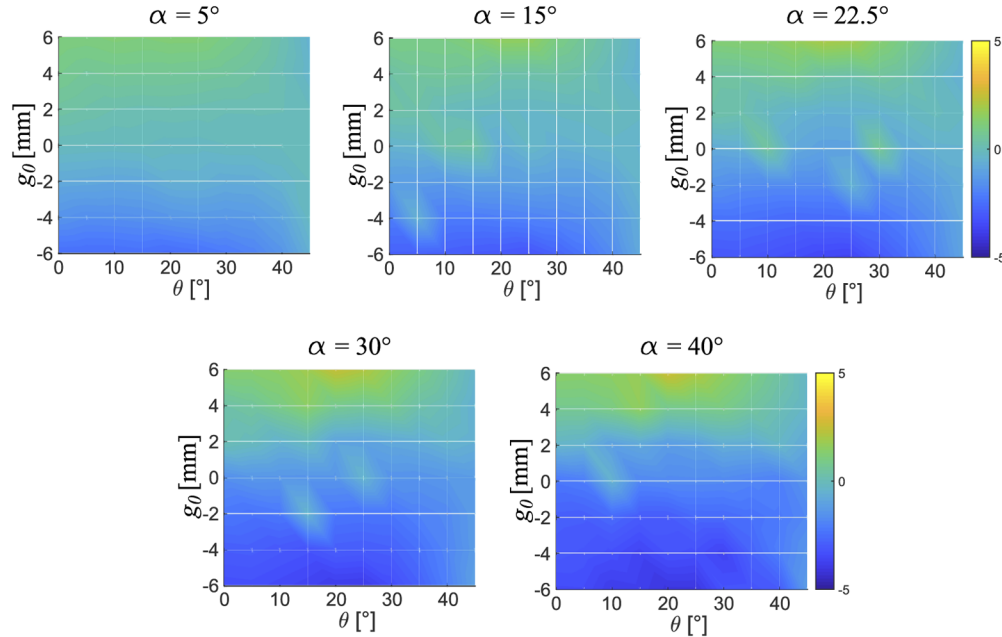


Fig. 4. Difference of the simulated and specified point of medium transmission $g_{0\text{sim}} - g_{0\text{spec}}$ for various g_0 , θ and α . Yellow coloration indicates that for this combination of g_0 and θ , the calculated $g_{0\text{sim}}$ exceeds the expected $g_{0\text{spec}}$, while blue coloration indicates that $g_{0\text{sim}} < g_{0\text{spec}}$. For an ideal α with every $g_{0\text{sim}}$ matching its corresponding $g_{0\text{spec}}$, the whole map would have the color of 0 mm deviation.

Using Fig. 4 and Fig. 5, we can therefore identify the electrode configuration with the least deviation for both $g_{0\text{sim}}$ and θ_{sim} by observing the color code. Overall, the negative values, i.e. the blue coloration is prevailing for $g_{0\text{sim}}$ while for θ_{sim} in Fig. 5, the areas of blue and yellow coloration are evenly balanced. This first impression is confirmed by the calculated average value of each map: While $\overline{g_{0\text{sim}} - g_{0\text{spec}}} = -0.5$ mm for $\alpha = 5^\circ$ and even reaches $\overline{g_{0\text{sim}} - g_{0\text{spec}}} = -1.2$ mm for $\alpha = 40^\circ$, it follows $\overline{\theta_{\text{sim}} - \theta_{\text{spec}}} \approx 0^\circ$ for all α . The negative deviations for $g_{0\text{sim}}$ may be explained by the asymmetric potential range of $\phi = [-1.6 \text{ V}, +0.5 \text{ V}]$ to which the working electrode potentials are restricted. The redox potential of the filter is $\phi_{\text{redox}} = -1.0 \text{ V}$ which means that the overall potential range for low transmission is smaller than that for high transmission. The simulated transmission profiles therefore tend to have larger colored areas than transparent areas which pushes the point of medium transmission further to the transparent area and thus to more negative values.

Concerning θ the deviations $\theta_{\text{sim}} - \theta_{\text{spec}}$ may not be small. However, they even out as we consider all angles between 0° and 45° . The contacts are evenly spaced so the next contact is located at 45° . This means due to symmetry the behavior in the range of $\theta = [0^\circ, 22.5^\circ]$ equals the inverted behavior in the range $\theta = [22.5^\circ, 45^\circ]$. We can further observe a trend to an increased deviation of $\theta_{\text{sim}} - \theta_{\text{spec}}$ when α is increased. The high deviations for $\alpha = 40^\circ$ are accompanied

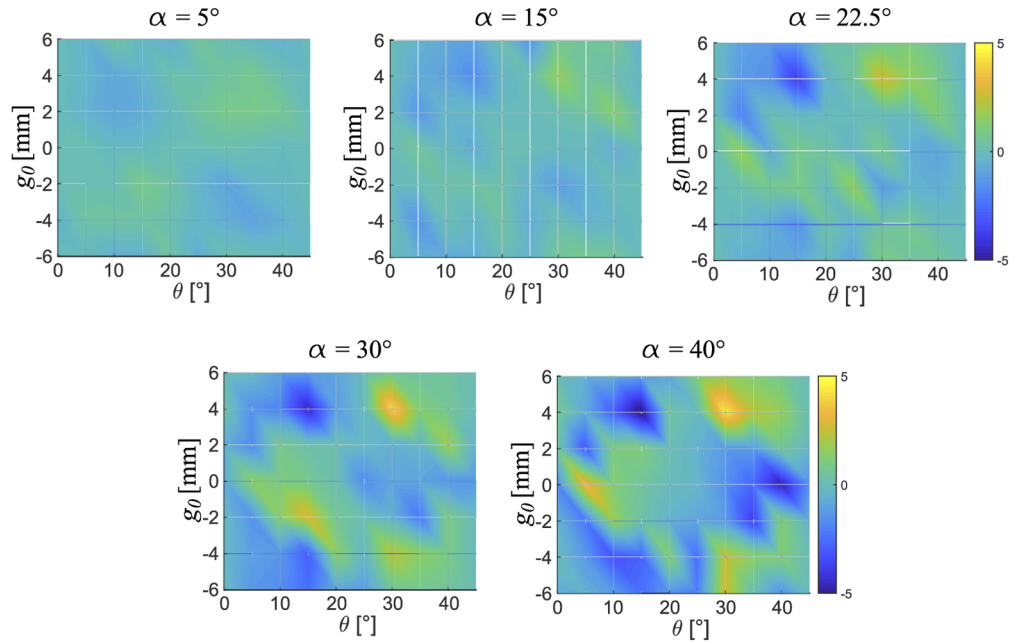


Fig. 5. Difference of the simulated and specified rotation of the gradient $\theta_{\text{sim}} - \theta_{\text{spec}}$ for various g_0 , θ and α . For an ideal α with every θ_{sim} matching its corresponding θ_{spec} , the whole map would have the color of 0° deviation.

by the low overall coefficient of determination and may as well be explained by the broad contact pads which distort the gradient at the edge of the optical area.

Until now, we have only focused on the influence of g_0 and θ . To investigate the parameter Δg , we study the transmission profile along the g -axis for varying Δg while keeping the other parameters fixed. Figure 6 shows the deviation $|T_{\text{sim}} - T_{\text{spec}}|$ and the coefficient of determination R^2 for different Δg and α . The deviations given by the colored graphs show the absolute values, so each profile along the g -axis has one point of zero deviation which is the crossing point of the T_{sim} and T_{spec} profiles. At y -positions around this crossing point, the highest deviations are found as the slopes of T_{sim} and T_{spec} disagree. However, at $y = -20$ mm and $y = 20$ mm, the deviations are small because both T_{sim} and T_{spec} reach the levels of high and low transmission.

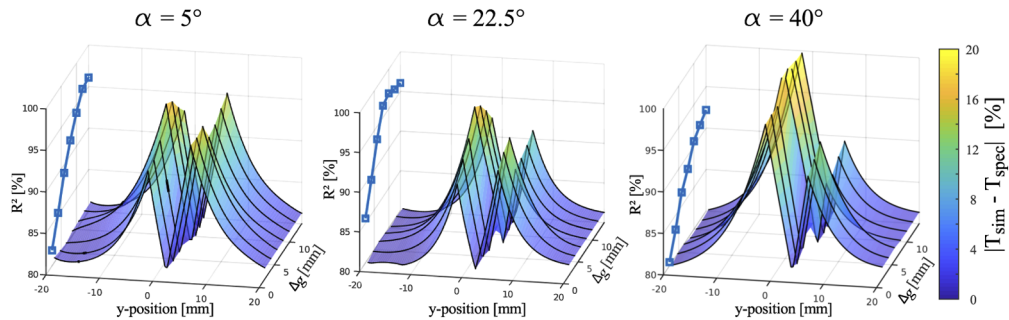


Fig. 6. Differences of the simulated and specified transmission along the y -axis for different widths of the transition zone Δg depicted in color code. Additionally, the coefficient of determination R^2 is given for seven different Δg values as blue line in the R^2 - Δg plane. In all simulations, the remaining parameters were kept at $g_0 = +2$ mm, $\theta = 0^\circ$ and $T_{\text{min}} = 10\%$.

In direct comparison of the three diagrams, it is apparent that the deviations for $\alpha = 40^\circ$ are the highest, reaching up to 20 %, while the diagram for $\alpha = 22.5^\circ$ shows the lowest deviations. This behavior also affects the coefficient of determination: $\alpha = 22.5^\circ$ has the highest correlation for all values of Δg . Generally speaking, small Δg produced the lowest correlation. This trend can be explained along with the results of Fig. 3: The steepest gradients, i.e. the gradients with the lowest Δg for a given ΔT , can be produced using medium values for α . This is why the correlation for $\alpha = 22.5^\circ$ in Fig. 6 stays at a high level until Δg falls below 6 mm, while for $\alpha = 5^\circ$ correlation starts to drop already for $\Delta g < 12$ mm. An explanation for this behavior may be that the area between contact pads is comparably large for $\alpha = 5^\circ$. The distance between the pads is a lower limitation for Δg . For very large α , the contact pads themselves are the limitation because they create an area of homogeneous potential and therefore a flat transmission profile.

Summarizing the results of the geometry optimization process, we can state that the first criteria, the correlation maps, gave the highest values of R^2 for $\alpha \leq 22.5^\circ$. The other two criteria, the deviations of $g_{0\text{sim}}$ and θ_{sim} , showed that while the average values had a satisfying agreement with the specifications, deviations increased with increasing α . When studying the impact of Δg , we found that $\alpha = 5^\circ$ tends to produce flat gradients and fails for $\Delta g < 12$ mm. The main finding is that $\alpha = 15^\circ$ and $\alpha = 22.5^\circ$ offer the best trade-off between a sufficient steepness of the gradient and a low variation at the edge of the optical area.

In a first application we manufactured an EC graduated filter with $\alpha = 22.5^\circ$ and applied the calculated potential combination (see Fig. 7). Unlike in our previous papers, the nanoparticle layers were deposited by a commercial gravure printing process. By adapting the amount of solvent in the nanoparticle paste, we obtained a viscosity of 100 mPa·s, which was suitable for printing. To achieve an overall nanoparticle layer thicknesses of $(2.0 \pm 0.1)\mu\text{m}$ ATO and $(2.4 \pm 0.4)\mu\text{m}$ TiO₂, we applied 6 single layers on both the TiO₂ working and the ATO counter electrode. This low variation in layer thickness of about 10 % results in an equally low variation of transmission in the homogeneously colored state. In comparison to the common doctor-blading process, gravure printing offers a better control of the nanoparticle layer thicknesses. This is because the roll used in the gravure printing process is laser engraved, so the depth of the gravure cells can be controlled individually, which enables a non-homogeneous application of the nanoparticle paste. As can be seen in Fig. 7(a)), the nanoparticle layers have a high transparency and good optical quality, which allows us to identify all logos of the participating partners on the background wall. The homogeneous coloration in Fig. 7(b)) emphasizes the homogeneous layer thickness and the high porosity of the layers which enable the dark coloration. One graduated state is portrayed in Fig. 7(c)), which shows an intermediate rotation of the filter ($\theta = 30^\circ$) at a medium $g_0 = +2$ mm and $\Delta g = 10$ mm. For the output of the eight potentials to the contact pads, we used a USB control module (USB-3114, Measurement Computing GmbH, Germany).

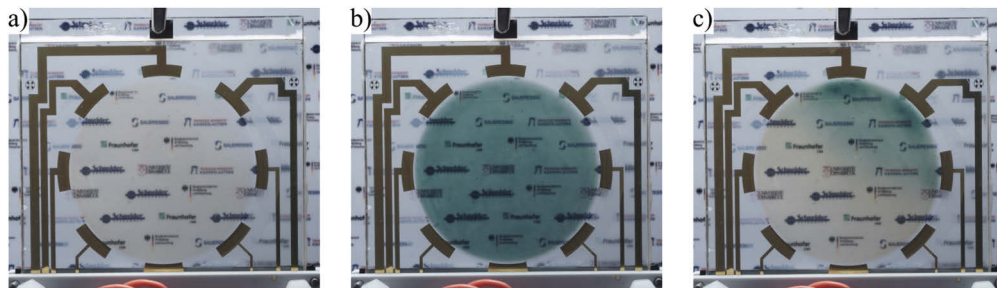


Fig. 7. Images of the manufactured EC graduated filter in the transparent state (a), the homogeneously colored state at -1.7 V (b) and in a graduated state (c) with $g_0 = +2$ mm, $\Delta g = 10$ mm, $T_{\text{min}} = 10\%$ and $\theta = 30^\circ$.

In this paper, we have presented a detailed geometry optimization of the contact pads for a two-dimensional EC graduated filter. With the chosen electrode opening angle $\alpha = 22.5^\circ$ we manufactured a functional device which confirms the previously simulated behavior. Using our simulation model and three criteria for the quality of the achievable graduated transmission, we were able to find the most promising electrode configuration which could be directly applied to the designated EC device.

Funding

Bundesministerium für Bildung und Forschung (13N14200, 13N14201, 13N14202, 13N14203, 13N14204, 13N14851).

Disclosures

The authors declare no conflicts of interest.

References

1. F. Banterle, A. Artusi, K. Debattista, and A. Chalmers, *Advanced High Dynamic Range Imaging* (Taylor & Francis Inc, 2017).
2. A. Serrano, F. Heide, and D. Gutierrez, "Convolutional Sparse Coding for High Dynamic Range Imaging," *Comput. Graph. Forum* **35**(2), 153–163 (2016).
3. R. Mortimer, D. Rosseinsky, and P. Monk, *Electrochromic Materials and Devices* (Wiley-VCH, 2015).
4. A. Kraft, "Electrochromism : a fascinating branch of electrochemistry," *ChemTexts* **5**(1), 1 (2019).
5. G. W. Kim, Y. C. Kim, I. J. Ko, J. H. Park, H. W. Bae, R. Lampande, and J. H. Kwon, "High-Performance Electrochromic Optical Shutter Based on Fluoran Dye for Visibility Enhancement of Augmented Reality Display," *Adv. Opt. Mater.* **6**(11), 1701382 (2018).
6. R. J. Mortimer, "Electrochromic Materials," *Annu. Rev. Mater. Res.* **41**(1), 241–268 (2011).
7. T. Deutschmann, C. Kortz, L. Walder, and E. Oesterschulze, "High contrast electrochromic iris," *Opt. Express* **23**(24), 31544 (2015).
8. A. Tsuboi, K. Nakamura, and N. Kobayashi, "Chromatic control of multicolor electrochromic device with localized surface plasmon resonance of silver nanoparticles by voltage-step method," *Sol. Energy Mater. Sol. Cells* **145**, 16–25 (2016).
9. A. Tsuboi, K. Nakamura, and N. Kobayashi, "Multicolor Electrochromism Showing Three Primary Color States Based on Size- and Shape-Controlled Silver Nanoparticles," *Chem. Mater.* **26**(22), 6477–6485 (2014).
10. G. A. Niklasson and C. G. Granqvist, "Electrochromics for smart windows : thin films of tungsten oxide and nickel oxide , and devices based on these," *J. Mater. Chem.* **17**(2), 127–156 (2007).
11. R. Kirchgeorg, S. Berger, and P. Schmuki, "Ultra fast electrochromic switching of nanoporous tungsten – tantalum oxide films," *Chem. Commun.* **47**(3), 1000–1002 (2011).
12. C. Kortz, A. Hein, M. Ciobanu, L. Walder, and E. Oesterschulze, "Complementary hybrid electrodes for high contrast electrochromic devices with fast response," *Nat. Commun.* **10**(1), 4874 (2019).
13. A. Hein, C. Kortz, and E. Oesterschulze, "Electrochromic tunable filters based on nanotubes with viologen incorporation," *Proc. SPIE* **10679**, 106791U (2018).
14. F. Campus, P. Bonhôte, M. Grätzel, S. Heinen, and L. Walder, "Electrochromic devices based on surface-modified nanocrystalline TiO₂ thin-film electrodes," *Sol. Energy Mater. Sol. Cells* **56**(3-4), 281–297 (1999).
15. P. Bonhôte, E. Gogniat, F. Campus, L. Walder, and M. Graetzel, "Nanocrystalline electrochromic displays," *Displays* **20**(3), 137–144 (1999).
16. M. Ciobanu, J. Klein, M. Middendorf, S. Mohsen, B. Mousavi, F. Carl, M. Haase, and L. Walder, "High contrast hybrid electrochromic film based on cross-linked phosphonated triarylamine on mesoporous antimony doped tin oxide," *Sol. Energy Mater. Sol. Cells* **203**, 110186 (2019).
17. U. zum Felde, M. Haase, and H. Weller, "Electrochromism of Highly Doped Nanocrystalline SnO₂:Sb," *J. Phys. Chem. B* **104**(40), 9388–9395 (2000).
18. A. Hein, C. Kortz, and E. Oesterschulze, "Tunable graduated filters based on electrochromic materials for spatial image control," *Sci. Rep.* **9**(1), 15822 (2019).